JOURNAL OF PETROLOGY

Journal of Petrology, 2016, Vol. 57, No. 7, 1389–1408
doi: 10.1093/petrology/egw044
Advance Access Publication Date: 9 August 2016
Original Article

OXFORD

Effect of Water Activity on Reaction Kinetics and Intergranular Transport: Insights from the $Ca(OH)_2 + MgCO_3 \rightarrow CaCO_3 + Mg(OH)_2$ Reaction at 1·8 GPa

Julien Gasc[1]*, Fabrice Brunet[2†], Nicolas Brantut[3], Jérôme Corvisier[4], Nathaniel Findling[2], Anne Verlaguet[5] and Christian Lathe[6]

[1]Laboratoire de Géologie, École normale supérieure, CNRS-UMR8538, Paris, France; [2]Université Grenoble Alpes, CNRS, ISTERRE, Grenoble, France; [3]Earth Sciences Department, University College London, London WC1E 6BT, UK; [4]Centre de Géosciences, Mines ParisTech, Fontainebleau, France; [5]ISTeP, Université Pierre et Marie Curie, 4 place Jussieu, Paris, France; [6]GFZ, Telegraphenberg, D-14473 Potsdam, Germany

*Present address: Géosciences Montpellier, Université de Montpellier-CNRS, Montpellier, France.
[†]Corresponding author. Telephone: +33 476 514 106. Fax: +33 476 635 252.
E-mail: fabrice.brunet@univ-grenoble-alpes.fr

Received January 16, 2015; Accepted June 6, 2016

ABSTRACT

The kinetics of the irreversible reaction $Ca(OH)_2 + MgCO_3 \rightarrow CaCO_3 + Mg(OH)_2$ were investigated at high pressures and temperatures relevant to metamorphic petrology, using both *in situ* synchrotron X-ray diffraction and post-mortem analysis of reaction rim growth on recovered samples. Reaction kinetics are found to strongly depend on water content; comparable bulk-reaction kinetics are obtained under water-saturated (excess water, *c.* 10 wt %) and under intermediate (0·1–1 wt % water) conditions when temperature is increased by *c.* 300 K. In contrast, similar reaction kinetics were observed at ~673 K and 823 K between intermediate and dry experiments, respectively, where dry refers to a set of experiments with water activity below 1·0 (no free water), as buffered by the $CaO–Ca(OH)_2$ assemblage. Given the activation energies at play, this gap—corresponding to the loss of no more than 1 wt % of water by the assemblage—leads to a difference of several orders of magnitude in reaction kinetics at a given temperature. Further analysis, at the microscopic scale, of the intermediate and dry condition samples, shows that intergranular transport of calcium controls the reaction progress. Grain boundary diffusivities could be retrieved from the classic treatment of reaction rim growth rate. In turn, once modeled, this rate was used to fit the bulk kinetic data derived from X-ray powder diffraction, offering an alternative means to derive calcium diffusivity data. Based on a comparison with effective grain boundary data for Ca and Mg from the literature, it is inferred that both dry and intermediate datasets are consistent with a water-saturated intergranular medium with different levels of connectivity. The very high diffusivity of Ca in the $CaCO_3 + Mg(OH)_2$ rims, in comparison with that of Mg in enstatite rims found by earlier workers, emphasizes the prominent role of the interactions between diffusing species and mineral surfaces in diffusion kinetics. Furthermore, we show that the addition of water is likely to change the relative diffusivity of Mg and Ca in carbonate aggregates. From a qualitative point of view, we confirm, in a carbonate-bearing system, that small water content variations within the 0–1 wt % range have tremendous effects on both intergranular transport mechanisms and kinetics. We also propose that the water content dependent diffusivity of major species (Mg, Ca) in low-porosity metamorphic rocks is strongly dependent on the interaction between diffusing species and mineral surfaces. This parameter, which will vary from one

rock-type to another, needs also to considered when extrapolating (P, T, t, $x\mathrm{H_2O}$) laboratory diffusion data to metamorphic processes.

Key words: metamorphic reaction; kinetics; intergranular transport; water; calcium diffusion

INTRODUCTION

The kinetics of metamorphic reactions is strongly dependent on temperature, grain size and water availability. The last parameter is probably the most difficult to quantify, especially over the course of a whole metamorphic cycle. The ubiquity of fluid during metamorphism has long been a subject of controversy (Thompson, 1983; Rubie, 1986) and it is now widely accepted that variations of water availability and content in metamorphic rocks are likely to account for the discrepancy between natural reaction kinetics and those extrapolated from experimental data (Baxter, 2003). In the field, the prominent role of water availability is supported by occurrences of partially eclogitized high-grade rocks in which eclogitization took place in shear zones, where fluid infiltrated (Austrheim, 1987; Molina *et al.*, 2002; John & Schenk, 2003). At a larger scale, by combining petrological and geophysical constraints, Hetenyi *et al.* (2007) have suggested that the eclogitization of the Indian lower crust beneath Tibet is delayed owing to equilibrium overstepping until it is catalyzed by the release of water from hydrous minerals.

Beyond the notion of water availability, which describes the intermittent presence of water in the course of the metamorphic reaction process, the question of the effect of water content on the reaction kinetics also appears to be relevant. In fact, most of the datasets of mineral reaction kinetics available in the literature (phase relationships, dissolution, etc.) are based on experiments performed under hydrothermal conditions with large water/rock ratios. Consequently, when extrapolated to nature, assuming permanent water availability, this type of experimental data predicts that metamorphic reaction rates are fast and that the preservation of metastable mineral assemblages (reaction equilibrium overstep) is short with respect to metamorphic timescales (Wood & Walther, 1983). Although possibly valid for metapelites transforming along their prograde path, this conclusion does not necessarily hold for high-grade rocks (e.g. upper amphibolite- or granulite-facies rocks) reacting back with water. In these latter circumstances, Yardley & Valley (1997) showed, on thermochemical grounds, that excess water conditions (i.e. water saturation) are not met and that water activity must be below unity (taking as the reference state pure water at T and P). In parallel, it has been shown recently that even minute amounts of water can have a drastic effect on the kinetics of mineral reactions through the enhancement of mass transport (Milke *et al.*, 2009, 2013; Carlson, 2010; Gardés *et al.*, 2012; Joachim *et al.*, 2012). In fact, a full range of intergranular diffusion regimes has been identified as a function of water content (Rubie, 1986; Farver & Yund, 1995) between the 'dry' and the 'water-saturated' end-member cases. These regimes are characterized by a range of grain boundary diffusivities that can span seven orders of magnitude in the case of aluminum (Carlson, 2010). Although Gardés *et al.* (2012) proposed a microscopic description for each of these intergranular diffusion regimes, the physical state of water below the 1 wt % level remains largely unknown under metamorphic pressures and temperatures. Furthermore, studies addressing the effect of low water contents on intergranular transport and its implications for mineral reaction rates are scarce although of high geological relevance. The *in situ* characterization at high pressure and temperature of the physico-chemical properties of intergranular water present in very low concentrations is obviously a difficult task. Gasc *et al.* (2011), for example, used *in situ* impedance spectroscopy at 2 GPa to characterize the electrical properties (diffusivity of electrical charge carriers) of the intergranular region of a brucite polycrystal as a function of temperature for various water contents. Using the CaO–$Ca(OH)_2$ and MgO–$Mg(OH)_2$ equilibria to buffer the water activity in the samples, Gasc *et al.* (2011) were able to show that grain boundary conductivity can vary by seven orders of magnitude as a function of water content. In our study we use a similar water buffering strategy to address the effect of low water content variation on intergranular transport in the course of the $Ca(OH)_2 + MgCO_3 \rightarrow CaCO_3 + Mg(OH)_2$ reaction at 1·8 GPa. Special attention is paid to bridging bulk and microscopic approaches so that reaction kinetics derived from time-resolved X-ray powder diffraction (XRPD) can be compared with the growth rate of $CaCO_3 + Mg(OH)_2$ rims around coarse magnetite ($MgCO_3$) grains dispersed in a fine portlandite [$Ca(OH)_2$] matrix. All terms and symbols used throughout the text are defined in Table 1.

EXPERIMENTAL METHODS

Experimental strategy

Cubic multi-anvil (MA) experiments were performed at 1·8 GPa at a range of temperatures (393–873 K), run durations and water contents on the non-reversible exchange reaction

$$Ca(OH)_2 + MgCO_3 \rightarrow Mg(OH)_2 + CaCO_3. \quad (1)$$

This reaction was chosen for its relatively fast kinetics, even under severely dry conditions, to allow investigation of its kinetics *in situ* from time-resolved

Table 1: Symbols used and their significance

Symbol	Description	Unit
T	Temperature	K
P	Pressure	Pa
t	Time	s
$\xi(t)$	Reaction progress (between zero and unity)	no unit
I_i	XRPD peak intensity; subscripts P and B refer to portlandite and brucite respectively	counts
χ_i	Weight proportion of phase i; subscripts P and B refer to portlandite and brucite respectively	no unit
ϕ	Calibration factor that relates phase proportion and selected Bragg's reflection intensity ratio	no unit
M_i	Molar weight of phase i; subscripts P and B refer to portlandite and brucite respectively	g mol^{-1}
J_i	Flux of species i	mol m^{-2} s^{-1}
D_{CaO}	CaO diffusion coefficient	m^2 s^{-1}
$\overline{D}_{CaO}$	Mean effective CaO diffusion coefficient across the reaction front or rim	m^2 s^{-1}
C_{CaO}	Concentration of CaO species	mol m^{-3}
R	Ideal gas constant	J mol^{-1} K^{-1}
μ^0_{CaO}	Chemical potential of CaO at the interface between portlandite and the reaction products (i.e. brucite and aragonite)	J mol^{-1}
μ'_{CaO}	Chemical potential of CaO at the interface between the reaction products (i.e. brucite and aragonite) and magnesite (see Fisler & Mackwell, 1994)	J mol^{-1}
$\Delta\mu_{CaO}$	CaO chemical potential difference across the reaction front or rim	J mol^{-1}
Δx	Reaction front (or rim) thickness	m
$\Delta_r G$	Gibbs free energy of the reaction	J mol^{-1}
$\overline{D}^{GB}_{CaO}$	Mean grain boundary diffusion coefficient of CaO across the reaction front or rim	m^2 s^{-1}
l	Grain size of the reaction products, brucite and aragonite, in the reaction front or rim	m
δ	Grain boundary width	m
V_i	Molar volume of phase i; subscripts r, m and p correspond to the reaction products (i.e. equimolar mix of aragonite and brucite), magnesite and portlandite, respectively	m^3 mol^{-1}
r_i	Radii used in the spherical geometry; subscripts A and B refer to the outer and inner radii of the reaction rim respectively and subscript 0 corresponds to the initial magnesite grain radius	m
V_r	Volume of the reaction rim; can be expressed as the difference between the volumes of the spheres having r_A and r_B for radii	m^3
n_i	Molar amount; subscripts p and m correspond to portlandite and magnesite, respectively	mol
ν	Ratio between molar volumes of magnesite and portlandite, V_m/V_p	no unit
$X(t)$	Reaction progress for a single coarse magnesite grain, between zero and unity	no unit
Port|Ara + Bru	Reaction interface with portlandite on one side and aragonite + brucite on the other	
n	Grain coarsening time exponent, equals three in our case	no unit
ρ	Grain coarsening constant; unit depends on n	m^3 s^{-1}
γ_0	Mean of the natural logarithm of the initial magnesite grain size (with radii log-normally distributed)	no unit
σ	Standard deviation of the natural logarithm of the initial magnesite grain size	no unit

synchrotron diffraction. Additional experiments were also performed in a piston-cylinder (PC) apparatus to investigate the kinetics of reaction (1) under water-saturated conditions at the same pressure, in sealed gold containers.

The recovered MA samples (i.e. dry and intermediate) were characterized using a Zeiss® field-effect scanning electron microscope (FE-SEM), which showed the presence of reaction rims around coarse residual magnesite grains. The kinetics of chemical transport across the rim-forming polycrystalline material, composed of brucite, $Mg(OH)_2$, and aragonite, $CaCO_3$, was characterized from the determination of rim growth rates as well as from one-dimension diffusion experiments performed with the same starting material in the PC apparatus. Grain boundary diffusion coefficients, $\overline{D}^{GB}\delta$, were retrieved from both datasets using a segregation factor set to unity, as major element diffusion is involved.

Finally, the two approaches (i.e. bulk reaction kinetics and chemical transport at the reaction rim scale) were bridged. Grain boundary diffusion coefficients were refined to fit the time-resolved synchrotron diffraction data; the diffusion coefficients obtained in this fashion were then compared with those retrieved from the growth rate of reaction rims and reaction fronts (FE-SEM data), to test the consistency between microscopic and bulk datasets.

Starting materials

The starting material was a mixture of natural magnesite, $MgCO_3$, and synthetic portlandite, $Ca(OH)_2$. Portlandite was synthesized hydrothermally (623 K, 150 MPa, 45 h) in a cold-seal vessel from CaO, which was obtained by decarbonation of reagent grade calcite (Merck 2066 with $<$1% impurities) at 1273 K. Magnesite was extracted from a natural single crystal containing less than 1 wt % CaO and FeO; the absence of mineral impurity was checked by XRPD. Portlandite and magnesite were ground together in an agate mortar in equimolar proportions. SEM observation showed that the starting material was composed of a fine-grained matrix (grain diameter less than 1 μm) with, sporadically, coarser magnesite grains (∼10 μm). These larger grains

are less reactive but, as described below, are suitable for the measurement of reaction rim growth rates.

Reaction kinetics from *in situ* synchrotron X-ray diffraction

High *P–T* experiments with *in situ* energy-dispersive XRPD were carried out using the MAX80 DIA press (six anvils cubic type multi-anvil) installed on beamline F2.1 at Hasylab. The starting powder was pressed to a pellet (2 mm in diameter) and fitted into a boron nitride (BN) sleeve, which chemically insulated the sample from the graphite furnace but was not designed to retain water. The BN sleeve was then fitted into a cylindrical graphite furnace and sandwiched between two dried NaCl pellets used as a pressure marker (Decker, 1971). Temperature was measured with a Type-N thermocouple, the junction of which was located at a NaCl–sample interface. Boron-epoxy cubes with 8 mm edges were used as the pressure medium in conjunction with 6 mm truncation WC anvils. Details of the cell assembly and the MAX80 press have been given by Mueller *et al.* (2003). It should be noted that to minimize X-ray absorption no sealed noble-metal container was used. Therefore, as described below, water-saturated experiments were achieved separately in the PC using sealed gold containers.

Two types of hydration levels were tested in the DIA experiments. The starting material was either equilibrated with the air moisture before being loaded into the BN sleeve, or was dried at 383 K and mixed with about 5 wt % CaO, a hygroscopic compound. In the former case, the amount of water adsorbed onto the starting material can be estimated by weight loss through heating at 383 K, and was found to reach *c.* 1 wt %. These hydration conditions are referred to below as intermediate. Gasc *et al.* (2011) showed, using *in situ* impedance spectroscopy on an $Mg(OH)_2$ aggregate at 2 GPa, that in a similar set-up where the sample is only partly sealed, such absorbed water mostly remains in the sample for several hours at temperature below *c.* 980 K. In the case where CaO (lime) was added to the oven-dried sample powder, residual free water from the sample and its close environment was removed below the set-point temperature by chemical drying following the reaction

$$CaO + H_2O \rightarrow Ca(OH)_2. \quad (2)$$

This method was successfully used by Gasc *et al.* (2011), who showed progressive sample drying, through CaO hydroxylation, as evidenced by a drop of the sample bulk electrical conductivity upon heating at temperatures as low as 673 K. Lime hydroxylation was similarly evidenced here by the pronounced decrease of the intensity of the CaO reflections upon heating at $T > 500$ K; that is, while the reaction of interest [reaction (1)] had not yet started (Fig. 1). As long as CaO and $Ca(OH)_2$ are present in the sample, the starting water activity is buffered to a value that depends on the free enthalpy of reaction (2) and therefore on temperature. The water activity was calculated using Wintwq 2.34 (Berman & Aranovich, 1996) in the 823–873 K temperature range corresponding to our experiments and was found to vary from 0·1 to 0·15. These experiments, which involve chemical drying, are termed dry in the subsequent discussion.

A white X-ray beam provided by the DORIS III storage ring was used to collect energy-dispersive XRPD

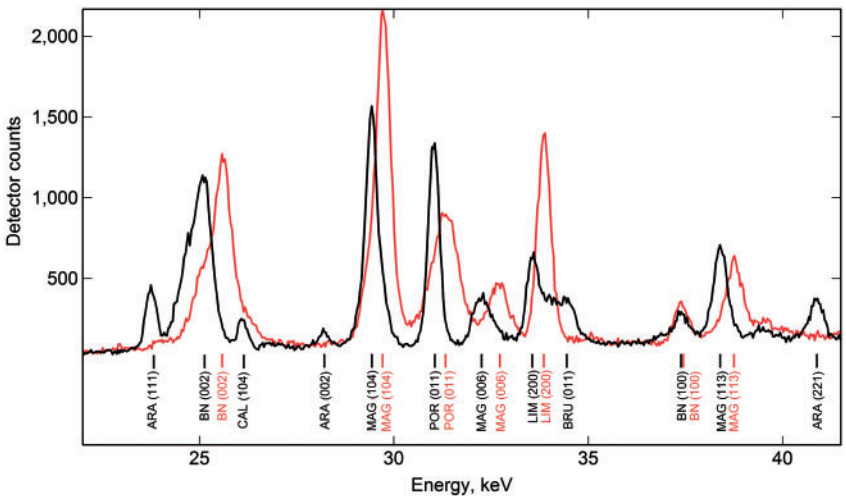

Fig. 1. XRPD patterns collected on sample Y13 showing the early water activity buffering of the lime–portlandite (LIM–POR) pair upon heating at 1·8 GPa. MAG, BRU, CAL and ARA stand for magnesite, brucite, calcite and aragonite, respectively. The red and black patterns correspond to data collected at room temperature and shortly before the target temperature of 833 K was reached, respectively. It should be noted that most peaks are shifted towards lower energies upon heating, as a result of thermal expansion. At *c.* 833 K upon heating, small amounts of reaction products (i.e. brucite and aragonite) are present along with minor transient calcite. The persistence of CaO is evidenced by its (200) reflection at 33·85 keV (black pattern), the intensity of which drastically decreased upon heating, as shown by the comparison between the red and black diffraction patterns, then remained constant during the rest of the experiment. The partial consumption of CaO is interpreted as resulting from the reaction with the sample and/or assembly water to form $Ca(OH)_2$. Numbers in parentheses are Miller indices of the diffracting planes.

data. The spectra were collected continuously with acquisition times of 45 or 60 s (Figs 1 and 2) with a 2048 channel solid-state Ge detector. The Bragg reflection of highest intensity typically varied from 2×10^3 to 5×10^3 detector counts.

Reaction progress $\xi(t)$ was calculated for each spectrum collected at a time t from the intensity $I(t)$ of selected diffraction peaks, assuming that $\xi(t) = I(t)/I_{max}$ for products and that $\xi(t) = 1 - [I(t)/I_{max}]$ for reactants, where I_{max} is the maximum intensity of the considered reflection (Zinn *et al.*, 1995; Lathe *et al.*, 2005). Therefore, for reactants at $t = 0$, $\xi(t) = 0$ and $I(0) = I_{max}$. We calculated reaction progress from the intensity of either the (104) reflection of $MgCO_3$ or the (011) reflection of $Ca(OH)_2$ (Fig. 2). Because of its larger grain-size distribution, magnesite is less suitable for quantification purposes using X-ray powder diffraction than portlandite, which was thus preferentially used to calculate $\xi(t)$. It should be noted that, with the use of white synchrotron light, the beam is collimated and the volume sampled is relatively small, which, in some cases, may translate as an insufficient number of grains sampled for proper quantitative analysis. This can cause the relative intensities of the diffraction peaks to fluctuate and not represent the actual phase proportions. Therefore, whenever possible, reaction progress was additionally retrieved from the (111) and (011) reflection intensities of $CaCO_3$ and $Mg(OH)_2$, respectively. In all cases for intensities I a background was also subtracted that was estimated for each t. The ratio between maximum peak intensity and background level was typically~30. In some instances, after collection of kinetic data at a certain constant temperature, the experiment was terminated by increasing further the temperature until $\xi(t) = 1$ was achieved,

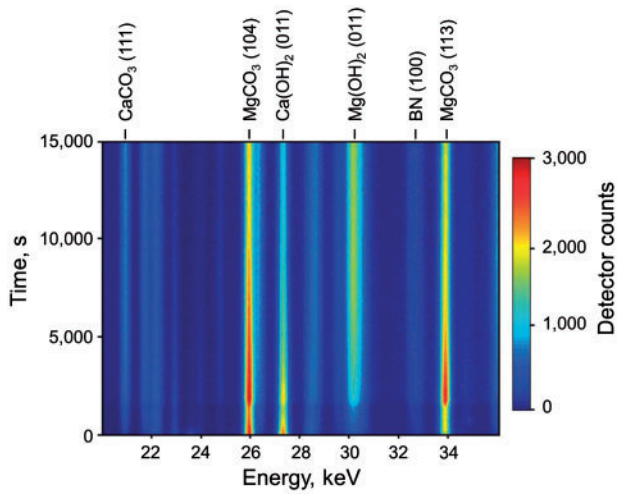

Fig. 2. *In situ* XRPD data for reaction (1) under intermediate conditions at 573 K and 1·8 GPa (run X15). The spectra were collected with a step time of 45 s. The main diffraction peaks are indexed, including reflections used for the calculation of reaction progress and the BN reflection used for intensity normalization. It should be noted that the corresponding diffraction energies differ from those in Fig. 1 owing to a different angle of the detector relative to the incident beam.

which allows retrieval of I_{max} values for the reaction products and allows their use for calculating $\xi(t)$. In addition, the incident beam intensity decayed with time owing to the decrease of the storage ring current. To account for this effect on peak intensities, and because the irradiated sample zone relative to the X-ray detector remains unchanged during an experiment, the peak intensities were normalized to the BN (100) reflection (Fig. 2).

Reaction kinetics with excess water

The kinetics of the reaction were also investigated at lower temperatures by performing off-beam PC experiments, for which both longer run durations and excess water (i.e. water-saturated) conditions could be more easily achieved. For these experiments, the solid starting material was loaded together with 10 wt % deionized water in a gold capsule which was then welded shut. These hydration conditions will be referred to below as saturated. Low-friction NaCl-based pressure cells (1/2 inch) were used. Further details on the pressure assembly have been given by Brunet *et al.* (2003). The temperature was measured with an S-type thermocouple and regulated within 1 K with a Eurotherm™ controller.

Angle dispersive XRPD patterns were collected on quenched products with a Rigaku diffractometer (Ultrax18hf-RINT2500) equipped with a Cu rotating anode (300 mA, 40 kV). XRPD data were collected using 0·02° steps at a speed of 2° min^{-1}. In this case, the reaction extent, $\xi(t)$, could be determined from reactant/product molar proportions in the quenched samples as follows. First, phase proportions were calculated using the relation

$$\frac{\chi_P}{\chi_B} = \varphi \frac{I_P}{I_B} \quad (3)$$

where φ is a constant, χ is the weight fraction of a given phase in the sample, I is the height (i.e. counts) of a selected diffraction peak, and the subscripts P and B stand for portlandite and brucite, respectively. The value of φ was calibrated from mixtures of known portlandite to brucite weight proportions using the height of the (001) reflection of each phase. The reaction progress, $\xi(t)$, corresponding to the molar fraction of the forming phase, brucite, was then estimated from the relation

$$\frac{\xi}{1-\xi} = \frac{\chi_B M_B}{\chi_P M_P} \quad (4)$$

where M_P and M_B are the molar masses of portlandite and brucite, respectively.

One-dimension diffusion experiments at intermediate hydration level

The kinetics of reaction (1) were further investigated in a one-dimension set-up using the piston-cylinder apparatus (1D-PC experiments) by measuring the width of the reaction zone that developed at the interface between

magnesite and portlandite polycrystals. This set-up aimed at characterizing grain-boundary transport with the simplest geometry. In contrast to the kinetic experiments described in the previous section, separate magnesite and portlandite powders (the same material as for the DIA and PC experiments, but unmixed) were loaded one after the other in a gold capsule. As much as possible, the contact between these two materials was made planar. No water was added to the capsule nor was the sample dried beforehand. The hydration level can therefore be considered here as intermediate. As for multi-anvil experiments, the run products of 1D-PC experiments were embedded in epoxy, cut and hand polished with diamond paste. After carbon coating, these samples were also characterized using the FE-SEM.

To investigate the temperature dependence of the chemical transport kinetics, these experiments were performed in the 773–873 K temperature range. Typical reaction front widths of ~1 mm were obtained for durations of several days.

EXPERIMENTAL RESULTS

Bulk kinetic data from time-resolved XRD

In total, 16 experiments were successfully performed on reaction (1) with time-resolved *in situ* XRPD at 1·8 GPa and for temperatures ranging from 573 to 873 K (Table 2). Each dataset is composed of tens to hundreds of diffraction patterns, each represented by a data point in Fig. 3. Water-saturated conditions were investigated at two temperatures (393 and 423 K) in four and five PC experiments (Fig. 3), respectively, which therefore correspond to two kinetic data points for saturated conditions in Fig. 4. Hundreds of PC experiments would have been required to achieve a time resolution on the reaction progress similar to that of the synchrotron-based experiments, which clearly emphasizes the advantage of using an *in situ* technique for kinetic purposes.

The scattering observed in the kinetic data obtained from synchrotron XRPD indicates a precision of ±10% on the reaction progress (Fig. 3). However, the precision on the reaction kinetics is better owing to the averaging of the large amount of data at each *P*–*T* condition. For PC experiments, the precision on the determination of the reaction progress is expected to be better than 5%; in particular, sample heterogeneity is averaged out by XRD patterns collected on a larger sample volume.

As can be observed from the shape of the reaction curves, the reaction rate is fastest when the reaction starts and slows down as the reaction proceeds. Heterogeneous reactions, such as the one studied here, do not generally comply with simple kinetic laws such as a zero- or first-order law. Furthermore, the presence of a grain-size distribution instead of single grain size in the starting material will influence the shape of the kinetic curve if the reaction process is dependent on the reactive surface area of the reactants. Finally, change of hydration conditions from one set of experiments to another may lead to a change in the reaction process (e.g. dissolution–crystallization in the water-saturated case). The overall shape of the kinetic curves can be successfully fitted to an empirical Avrami law (Avrami, 1939) with an exponent value of 0·4, which, according to Christian (1975), would reflect a diffusion-limited reaction process. However, owing to the truly empirical character of these fits, following Brown *et al.* (1962), we decided to merely compare half-reaction times (i.e. the time needed to reach $\xi = 0{\cdot}5$) between all datasets to grasp the effect of water as a whole on the reaction kinetics (Table 2, Fig. 4). It should be noted that for the particular case of the PC experiments performed with 10 wt % water (water-saturated conditions), a dissolution–precipitation process is expected to occur. However, aqueous species transport rate—rather than dissolution rate—may well be the rate-limiting process. Diffusivity of aqueous species in bulk water is not within the scope of the present study. These 'saturated' experiments should be seen as representative of the water-excess experiments usually carried out in experimental petrology.

Both series of experiments performed under dry and intermediate conditions seem to display an Arrhenius-type behavior (i.e. the logarithm of half-reaction times has a linear dependence on reciprocal temperature), although, comparatively, experimental data obtained for an intermediate hydration level are much more scattered (Fig. 4). The dependence of the reaction kinetics on water content is probably causing the important scattering observed in the intermediate dataset (see Discussion section). The present results illustrate a marked effect of water content on the kinetics. We note that similar half-reaction times (*c.* 1 h) were obtained at ~823, 648 and 423 K, for dry, intermediate and saturated conditions, respectively, although the gap between intermediate and dry conditions seems to shrink towards higher temperatures owing to an apparently larger activation energy of the kinetics under dry conditions.

Chemical transport through the $CaCO_3 + Mg(OH)_2$ reaction rims

FE-SEM images of the recovered 1D-PC samples show mineral intergrowth in reaction zones composed of $Mg(OH)_2$ and $CaCO_3$ (Fig. 5a). Energy-dispersive spectrometry data collected with the FE-SEM indicated that the Ca/(Ca + Mg) molar ratio remains constant and equal to 0·5 across the reaction zones. In all of the DIA samples, partly reacted magnesite grains are surrounded by reaction rims (Fig. 5b) within which the grain size of the reaction products is found to gradually increase from the Ara + Bru|Mag interface to the Port|Ara + Bru interface. These reaction rims are composed of equimolar $Mg(OH)_2$ (brucite) + $CaCO_3$ (aragonite) and show the same textural characteristics (grain-size distribution, symplectite intergrowth) as the reaction fronts in 1D-PC experiments. For 1D-PC and DIA experiments, the grain

Table 2: Experimental conditions, bulk kinetics and reaction rim growth data, and corresponding diffusivity parameters

Dataset*	Peaks used (bulk)	T (K)	t (s)	$t(\xi = 0{\cdot}5)$ (s)	$\Delta_r G$ (kJ mol^{-1})	ρ (m^3 s^{-1})	$D^{GB}\delta \pm 1\sigma$ (m^3 s^{-1}; bulk)	Δx† (μm)	r_A (μm)	r_B (μm)	$D^{GB}\delta \pm 1\sigma$ (m^3 s^{-1}; micro‡)
DIA, dry											
X07	Por Bru	873	1499	4·50E + 01	−41·3	—	2·28E − 21 ± 4·3E − 20	—	—	—	—
X08	Mag Bru Ara	843	6759	1·90E + 02	−41·6	—	4·81E − 22 ± 9·2E − 21	—	—	—	—
X09	Mag Bru Ara	823	9911	5·10E + 03	−42·0	—	9·77E − 24 ± 1·9E − 22	—	3·6	1·9 ± 0·1	9·72E − 24 ± 1·5E − 24
Y11	Por Bru	833	10160	4·20E + 02	−41·9	—	2·10E − 22 ± 4·0E − 21	—	—	—	—
Y13	Por Bru	833	9927	1·90E + 03	−41·9	—	2·57E − 23 ± 4·9E − 22	—	—	—	—
AA12	Mag Bru Ara	853	279	6·00E + 00	−41·6	—	9·49E − 21 ± 1·8E − 19	—	5·1	2·3 ± 0·1	4·44E − 22 ± 5·6E − 23
AA13§	—	823	1064	—	−42·0	—	—	—	6·8	2·3 ± 0·1	2·50E − 22 ± 3·1E − 23
DIA, intermediate											
X10	Por Bru	823	816	2·00E + 00	−42·0	2·72E − 22	1·54E − 20 ± 2·2E − 19	—	—	—	—
X11	Por Bru	673	8739	4·80E + 02	−43·2	3·60E − 26	7·94E − 24 ± 1·1E − 22	—	5·0	2·4 ± 0·2	6·76E − 25 ± 1·0E − 25
X12	Por Bru	743	408	1·40E + 00	−42·8	3·64E − 24	2·47E − 21 ± 3·5E − 20	—	—	—	—
X15	Por Bru	573	14866	2·80E + 03	−43·6	6·97E − 30	3·31E − 26 ± 4·7E − 25	—	—	—	—
Y09	Por Bru	623	6267	1·24E + 06	−43·5	7·06E − 28	1·17E − 26 ± 1·7E − 25	—	—	—	—
Y10	Por Bru	598	8918	2·16E + 06	−43·5	7·72E − 29	4·11E − 27 ± 5·8E − 26	—	—	—	—
Y14	Por Bru	673	3131	9·10E + 02	−43·2	3·60E − 26	1·28E − 24 ± 1·8E − 23	—	—	—	—
AA9	Mag Bru Ara	648	5730	1·60E + 05	−43·3	5·44E − 27	3·98E − 26 ± 5·6E − 25	—	10·0	9·0 ± 0·3	7·04E − 26 ± 6·7E − 27
AA10	Mag Bru Ara	723	4184	1·40E + 04	−42·9	1·07E − 24	1·28E − 24 ± 1·8E − 23	—	15·0	12·3 ± 0·1	4·07E − 24 ± 9·0E − 26
AA11	Mag Bru Ara	648	5218	9·80E + 03	−43·3	5·44E − 27	2·51E − 25 ± 3·5E − 24	—	5·0	4·4 ± 0·1	2·64E − 26 ± 1·7E − 27
1D-PC, intermediate											
PC182	—	823	234000	—	−42·0	2·72E − 22	—	850 ± 75	—	—	4·26E − 19 ± 1·2E − 19
PC180	—	773	1897200	—	−42·5	2·04E − 23	—	280 ± 62	—	—	4·48E − 21 ± 3·9E − 21
PC175	—	873	259200	—	−41·3	2·70E − 21	—	1380 ± 125	—	—	2·43E−18 ± 6·9E−19
PC, saturated											
PC_120	Por Bru	393	—	2·16E + 04	—	—	—	—	—	—	—
PC_150	Por Bru	423	—	6·00E + 03	—	—	—	—	—	—	—

*Each intermediate and dry condition DIA dataset corresponds to a single experiment, whereas each of the two PC saturated datasets corresponds to a series of quench experiments. The 1D-PC data in intermediate conditions also correspond to single experiments (see experimental section for details).
†Uncertainties on measurements of reaction front length and rim radii are given as ± 1σ. Error on r_A is the same as for r_B.
‡Most experiments were terminated by increasing the temperature until full reaction completion was observed, which does not allow those samples to be used for the microscopic approach.
§AA13 was run offline (without synchrotron XRPD) and was therefore not used in the bulk approach. It should be noted that $l = 120$ nm.

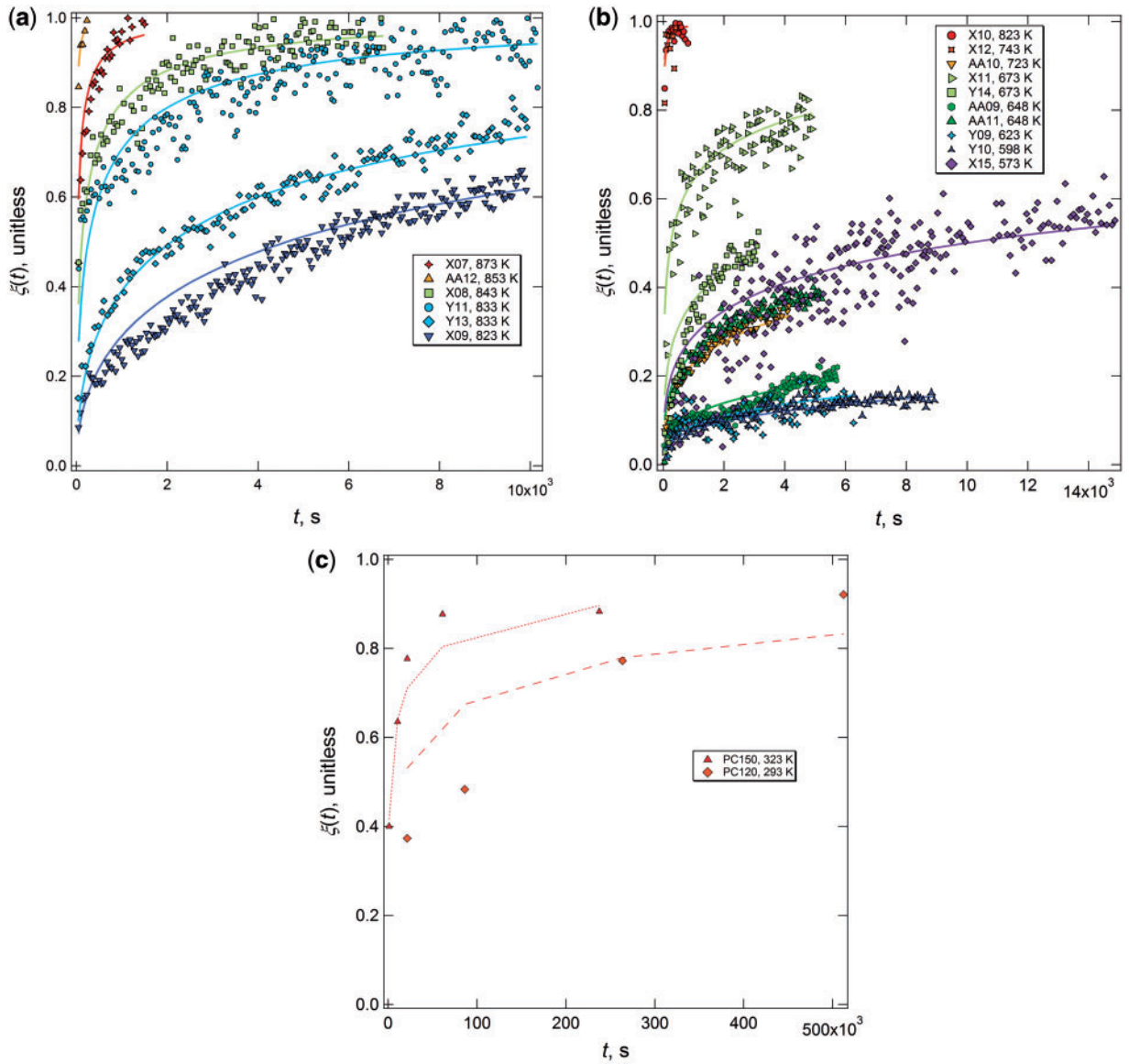

Fig. 3. Bulk kinetic data (reaction progress) and simulated kinetic curves. (a) Dry conditions (DIA); (b) intermediate conditions (DIA); (c) saturated conditions (PC). Reaction progress data were obtained from diffraction reflection relative intensities for (a) and (b) (see text for details) and from equation (4) for (c).

size of the reaction products varies between 30 nm and a few micrometers (Fig. 5d and e), depending on temperature, water content and run duration. The constant stoichiometry ($CaO/H_2O = MgO/CO_2 = 1$) throughout the reaction zones in both 1D experiments and DIA samples, implies the equality of Ca (CaO) and H (H_2O) fluxes through the Port|Ara + Bru interface. Similarly, the Mg (MgO) and C (CO_2) fluxes must be identical through the Ara + Bru|Mag interface. In experiment PC_180, a Pt chip was positioned at the interface between portlandite and magnesite. The Pt chip (Fig. 5a) remained at the Port|Ara + Bru interface in the course of the diffusion process. Its presence at the interface appears to have hindered the transport of species from the Port|Ara + Bru interface to the Ara + Bru|Mag interface, as indicated by the depression of the reaction front opposite to the Pt chip. Therefore, CaO and H_2O are the mobile species in the system, whereas MgO and CO_2 remained comparatively immobile. This conclusion is in line with the grain-size gradient observed across the reaction zones, where grains situated next to the Port|Ara + Bru interface formed first and are therefore larger.

$\overline{D}_{CaO}$ retrieval from 1D experiments

We showed in the previous section that the reaction zone growth in 1D-PC and DIA samples is controlled (i.e. limited) by the diffusion of CaO, assuming that H_2O diffusion is not limiting. The growth rate of the reaction zone (front or rim) depends on the molar flux of the limiting diffusing species (i.e. J_{CaO} in the present case) perpendicular to the reaction zone. Let us consider an equimolar mix of brucite and aragonite as a single phase having an effective molar volume corresponding

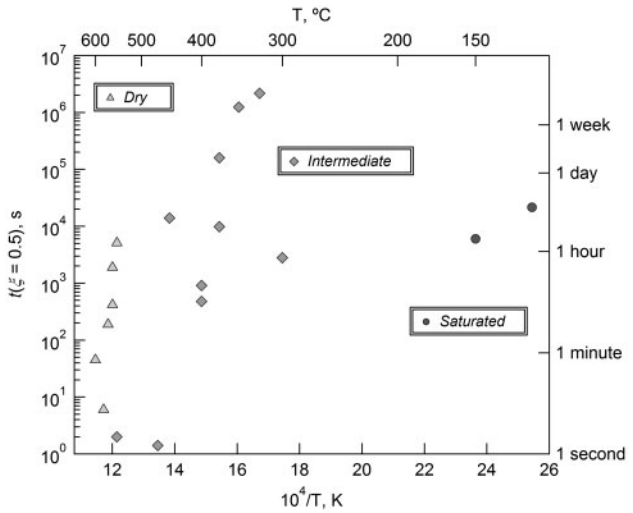

Fig. 4. Half-reaction times obtained from all 16 DIA experiments as well as from the two sets of PC experiments, at 393 and 423 K. Values are plotted on a logarithmic scale vs reciprocal temperature. Usual time measures are given as a guide to comprehend the tremendous effect of temperature on the kinetics, which range from seconds to weeks within less than a 200 degree temperature span. Triangles, diamonds and circles stand for dry, intermediate and water-saturated conditions, respectively.

to V_r (Fig. 6a). In the planar geometry of our 1D-PC experiments, because each mole of CaO diffusing through the front results in the creation of 1 mole of the said hypothetical phase, the growth rate of the reaction front thickness, Δx, can be written

$$\frac{d\Delta x}{dt} = J_{CaO} V_r. \quad (5)$$

According to the formalism developed by Fisler & Mackwell (1994), Fick's first law for diffusion can be used to write the CaO flux across the reaction zone, J_{CaO}, as a function of the CaO chemical potential gradient, $d\mu_{CaO}/dx$, as follows:

$$J_{CaO} = -\frac{D_{CaO} C_{CaO}}{RT} \frac{d\mu_{CaO}}{dx}. \quad (6)$$

Fisler & Mackwell (1994) also showed that this latter expression can be integrated using the mean-value theorem, introducing the mean diffusion coefficient, $\overline{D}_{CaO}$, which represents the mean value for diffusion across the reaction front or rim. The flux can then be written

$$J_{CaO} = -\frac{\overline{D}_{CaO} C_{CaO}}{RT} \frac{\Delta\mu_{CaO}}{\Delta x} \quad (7)$$

where $\Delta\mu_{CaO} = \mu'_{CaO} - \mu^0_{CaO}$ and therefore represents the chemical potential difference across the reaction zone.

Let us now consider the Ara + Bru|Mag interface, where, by definition, $x = \Delta x$ (Fig. 6a). If we consider the equilibrium between $MgCO_3$, the reaction products and the diffusing components, CaO and H_2O, we can write that

$$\mu_{MgCO_3} + \mu'_{CaO} + \mu'_{H_2O} = \mu_{Mg(OH)_2} + \mu_{CaCO_3}. \quad (8)$$

In addition, at $x = 0$, $\mu^0_{CaO} = \mu_{Ca(OH)_2} - \mu^0_{H_2O}$. Assuming that water activity is constant across the whole sample (owing to supposedly faster diffusion kinetics), then $\mu^0_{H_2O} = \mu'_{H_2O}$. We can therefore write

$$\mu'_{H_2O} = \mu_{Ca(OH)_2} - \mu^0_{CaO} \quad (9)$$

Finally, combining equations (8) and (9) gives

$$\mu'_{CaO} - \mu^0_{CaO} = \mu_{Mg(OH)_2} + \mu_{CaCO_3} - \mu_{MgCO_3} - \mu_{Ca(OH)_2} \quad (10)$$

from which we find that $\Delta\mu_{CaO} = \Delta_r G$. In addition, it should be noted that, in the present case, $C_{CaO} V_r = 1$. The combination of (5) and (7) then yields

$$\frac{d\Delta x}{dt} = -\frac{\overline{D}_{CaO}}{RT} \frac{\Delta_r G}{\Delta x}. \quad (11)$$

We note here that the mean diffusion coefficient, $\overline{D}_{CaO}$, is an effective (i.e. apparent) diffusion coefficient, considering the brucite + aragonite aggregate in the reaction zone as a homogeneous diffusing medium. Effective and grain boundary diffusion coefficients are related to one another by a ratio that depicts the shape and the volume fraction of grain boundaries available for intergranular diffusion. For example, in the ideal case where grain boundaries are planar (i.e. devoid of tortuosity) and parallel to the diffusion flux, the following relation applies (Brady, 1983):

$$\overline{D}^{GB} = \overline{D} \frac{2l}{\pi\delta} \quad (12)$$

where l is the distance separating the diffusion planes (i.e. the grain size; Fig. 6a), and δ is the grain boundary width. Because this latter parameter is virtually impossible to determine, most researchers choose to report the product of the grain boundary diffusivity $\overline{D}^{GB}$ and the grain boundary width, δ. However, during the diffusion process and the growth of reaction rims or fronts, l is not constant but obeys an exponential grain growth law (Joesten, 1991):

$$l = (\rho t)^{1/n} \quad (13)$$

where ρ and n are the grain coarsening rate constant and exponent, respectively. Combining relations (12) and (13) yields the expression

$$\overline{D}^{GB} = \overline{D} \frac{2(\rho t)^{1/n}}{\pi\delta}. \quad (14)$$

It has been shown that the growth of reaction fronts limited by grain boundary diffusion is no longer proportional to the square root of time, but that it slows down further with time owing to grain coarsening, and therefore decreasing availability of grain boundaries (Gardés & Heinrich, 2011). In that case, Δx is proportional to $(t^{1-1/n})^{1/2}$, where n is the grain coarsening exponent. Here, the combination of equations (11) and (14) gives the relation between rim thickness and

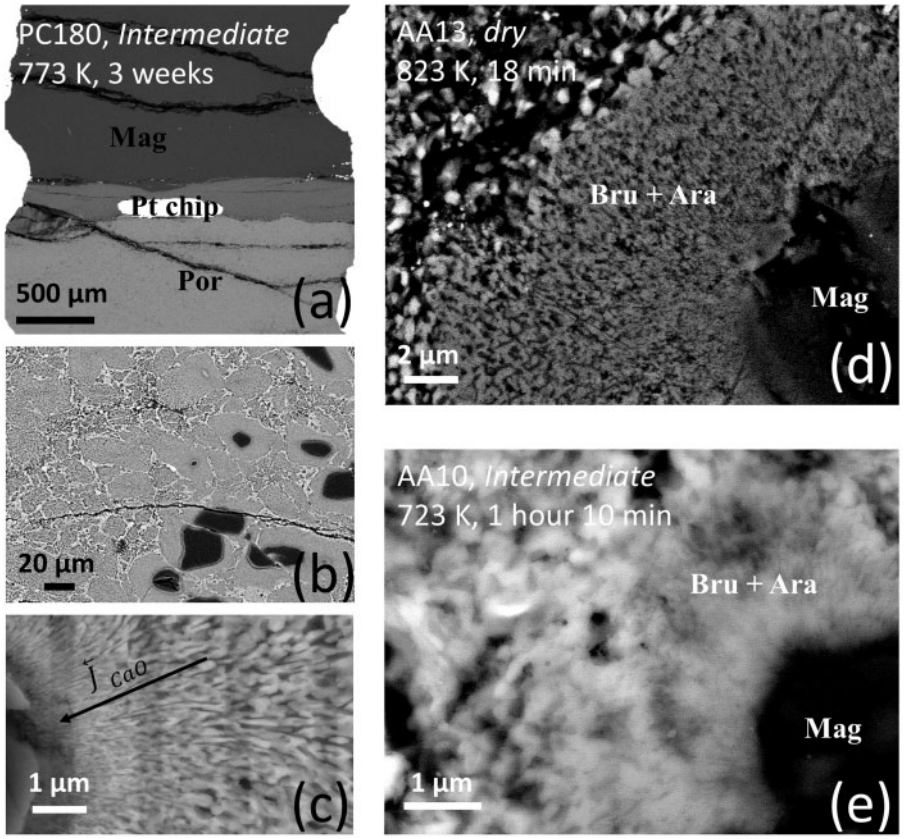

Fig. 5. FE-SEM images in back-scattered electron (BSE) mode of recovered samples. Abbreviations Por, Mag, Bru and Ara stand for portlandite, magnesite, brucite and aragonite respectively. (a) 1D-PC sample PC180. The reaction front between portlandite (lower, bright phase) and $MgCO_3$ (upper dark phase) is visible. The Pt chip (white color) is at the Port|Ara + Bru interface. The fracture network formed upon sample decompression and was not present when the sample reacted. (b) and (c) DIA samples Y10 and Y11, respectively. After collection of the kinetic data (shown in Fig. 3) the temperature was increased for both samples to ~1073 K (see experimental section for details). (b) As a result these samples show large reaction rims around the coarsest residual magnesite grains. (c) Also owing to higher temperatures, well-defined palisade-type rims with brucite and aragonite (darker and brighter phases, respectively) intergrowths are observed. The edge of a residual magnesite grain is visible in the lower left corner. (d) and (e) Detailed views of reaction rims in samples AA13 and AA10, respectively. The reacting magnesite grain is visible in the bottom lower corner in both cases. The finer grain size of the reaction products in (e), owing to a lower temperature, should be noted.

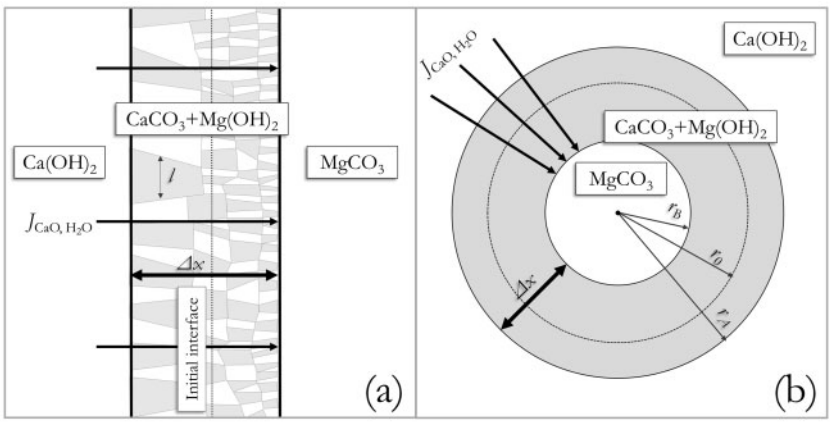

Fig. 6. Idealized geometries used for the calculation of $\overline{D}^{GB}_{CaO}\delta$. (a) Planar geometry used for calculations of diffusion coefficients from reaction front thickness (1D-PC experiments). (b) Spherical geometry used for the calculation of $\overline{D}^{GB}_{CaO}\delta$ from reaction rim dimensions (DIA experiments, microscopic approach) and using the analytical solution derived from Abart *et al.* (2009) to fit the kinetic curves (DIA experiments, bulk approach).

time as a function of the grain boundary diffusion coefficient:

$$\frac{\mathrm{d}\Delta x}{\mathrm{d}t}\Delta x = -\overline{D}^{\mathrm{GB}}\delta\frac{\Delta_{\mathrm{r}}G}{RT}\frac{\pi}{2\rho^{1/n}}t^{-1/n}. \quad (15)$$

Integrating the above equation, noting that for $t=0$ then $\Delta x=0$, we obtain the relation

$$\Delta x = \sqrt{\left[-\overline{D}^{\mathrm{GB}}\delta\frac{\Delta_{\mathrm{r}}G}{RT}\frac{\pi}{\rho^{1/n}}\left(\frac{n}{n-1}\right)\right]}t^{(n-1)/2n}. \quad (16)$$

In the present case (see Appendix A), the grain size of the reaction products was analyzed using SEM imaging to constrain the grain coarsening parameters, ρ and n. Equation (16) was then used to derive $\overline{D}^{\mathrm{GB}}\delta$ from 1D-PC experiments (Table 2), where a planar geometry applies (Fig. 6a).

Generally speaking, the presence of water may affect $\overline{D}_{\mathrm{CaO}}$ values by affecting any of the other parameters included in equation (14), specifically CaO mobility in the intergranular medium (i.e. $\overline{D}^{\mathrm{GB}}_{\mathrm{CaO}}$), grain boundary width and grain growth. This holds for experimentally grown coronae and also for natural metamorphic reactions as well, and because these latter parameters are difficult to estimate, one might also want to compare effective diffusivity values, $\overline{D}_{\mathrm{CaO}}$. This approach was chosen by Carlson (2010), where Al effective diffusion coefficients were retrieved in the case of natural metamorphic coronae; it allows evaluation of the overall effects of water content variations on the growth of reaction zones and visualization of how they affect metamorphic reaction kinetics in general.

$\overline{D}_{\mathrm{CaO}}$ retrieval from reaction coronae (spherical setting)

Similar to our 1D-PC experiments, SEM examination of the DIA samples showed that the reaction proceeds via the development of reaction rims around magnesite grains. This is well illustrated by the coronae observed around coarser residual magnesite grains in some samples (Fig. 5b). The dimensions of these reaction rims can be used to calculate effective diffusion coefficients according to the model shown in Fig. 6b. We note, however, that in the initial setting (at $t=0$) magnesite grains are not surrounded strictly by portlandite only, but rather by a mix of finer magnesite grains and portlandite. This may result in low Ca availability for diffusion and growth of the reaction rims, which, in turn, implies that the diffusion values retrieved may be underestimated. Unfortunately, it is impossible to measure the impact of this bias on the values retrieved.

The spherical setting implies that equations (5)–(7) defined above in a planar setting no longer apply. We used the analytical solution given for a spherical geometry by Abart *et al.* (2009) that relates the rim dimensions and the bulk diffusion coefficient. This relation was modified to take grain coarsening for intermediate conditions into account; the dry case was treated assuming constant grain size in the rim (see below and Appendix A for details).

It should be noted that rim widths are determined from SEM images of sample sections that do not necessarily pass through the center of the imaged magnesite grains. This can introduce a measurement bias with apparently larger $r_{\mathrm{A}}/r_{\mathrm{B}}$ ratios. Therefore, as much as possible, only rims with the lowest $r_{\mathrm{A}}/r_{\mathrm{B}}$ ratio were used for the present determination (i.e. largest residual grains were preferentially picked). Additional errors may arise from the estimation of the inner and outer rim dimensions, r_{B} and r_{A} respectively (see Table 2). Errors on those measurements are of 0·1–0·3 μm (Table 2). According to equation (A5), $\overline{D}^{\mathrm{GB}}_{\mathrm{CaO}}\delta$ is proportional to the square of r_{B}/r_0, which is accounted for by the error bars in the Arrhenius plot (Fig. 7a).

Diffusivity values obtained for both 1D-PC and DIA (3D) experiments are listed in Table 2 and are reported in Fig. 7a (open symbols). We note that the intermediate data retrieved from 1D-PC and DIA experiments, although conducted over very different time scales (i.e. a few hours and several days respectively), show a good consistency. Despite the uncertainties discussed above, the results clearly show a gap between dry and intermediate conditions, where comparable diffusivities are found at 823 and 673 K, respectively.

Numerical extraction of diffusivity values from bulk reaction kinetics

The bulk reaction progress, $\xi(t)$, represents the molar fraction of magnesite (or portlandite) which reacted after a given run duration. At the scale of a single magnesite grain surrounded by portlandite, the reaction progress, $X(t)$, is related to the inner rim radius, r_{B}, as follows:

$$X(t) = 1 - \frac{{r_{\mathrm{B}}}^3}{{r_0}^3} = 1 - y^3. \quad (17)$$

If reaction rim growth is the limiting factor to the bulk reaction progress, then reaction kinetics derived from *in situ* diffraction should correspond to the magnesite rim growth kinetics [i.e. $X(t)=\xi(t)$]. However, the relation between $\xi(t)$ and $X(t)$ depends on the magnesite grain-size distribution. SEM images show that this distribution consists of a fine-grained fraction (<1 μm) along with coarser grains, the size of which can be as large as several tens of microns. We assumed a log-normal grain-size distribution, typical of ground powders (Astrom, 2006; German, 2009; Sanchidrian *et al.*, 2012), characterized by γ_0 and σ, which represent respectively the mean and the standard deviation of the grain-size natural logarithm. The grain-size distribution was binned into 25 grain sizes with corresponding proportions (p_i). Using, again, the analytical solution derived from Abart *et al.* (2009) in equation (A5), we could simulate reaction progress data, $X_i(t)$, for each grain size. Then kinetic curves [i.e. $\xi(t)$] were obtained by calculating the weighted sum $\sum_{i=1}^{25} p_i X_i(t)$ with

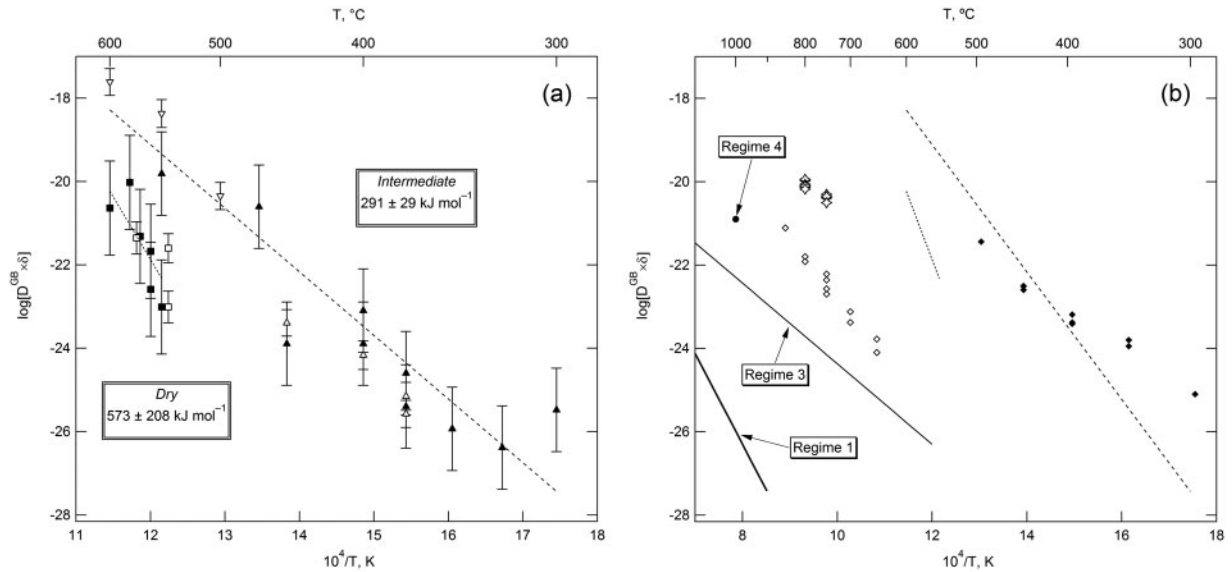

Fig. 7. Summary of the $\overline{D}^{GB}_{CaO}\delta$ values obtained in this study and comparison with literature data. (a) Triangles and squares correspond to intermediate and dry data, respectively. Open symbols represent values retrieved from SEM measurements of reaction rim widths for both intermediate and dry conditions (microscopic approach) with down-pointing triangles representing the 1D-PC data obtained under intermediate conditions. Diffusion data extracted from reaction progress vs time curves are reported with filled symbols (bulk approach). The dashed lines represent Arrhenius laws obtained by least-squares fitting of the dry and intermediate data; the activation energies and their respective uncertainties are indicated. (b) The Arrhenius laws corresponding to our data and shown in (a) are reported here (dashed lines) along with grain boundary diffusion data for carbonates from the literature: Farver & Yund (1996), Ca diffusion in calcite (open diamonds); Farver & Yund (1998), O diffusion in calcite (filled diamonds); Helpa *et al.* (2014), Ca diffusion during dolomite rim growth (open stars). Additional data were added to illustrate the previously demonstrated effect of water content: the black and grey curves and the filled circle represent diffusion regimes 1, 3 and 4 for Mg in enstatite grain boundaries, as defined by Gardés & Heinrich (2011) and Gardés *et al.* (2012); these correspond to dry conditions and 0·1–0·5 wt % and 2·1 wt % water, respectively.

$\sum_{i=1}^{25} p_i = 1$. For each experimental dataset, this approach was used to simulate kinetic data with varying values of $\overline{D}^{GB}_{CaO}\delta$. The best fit to the experimental data was then obtained using a standard grid search algorithm and by minimizing the absolute value of the difference between modeled and observed kinetic curves; this method is also known as the least absolute deviations (LAD) method. The uncertainty on $\overline{D}^{GB}_{CaO}\delta$ introduced by possible error on the initial grain-size distribution is addressed in Appendix B. It should be noted here, that, as mentioned in the Experimental Methods section, the diffraction peak intensities used to calculate reaction progress may not reflect the actual proportion of a phase in the sample at a given time, but may differ significantly. Based on observations of the standard deviation in our DIA datasets, we inferred that this bias could result in errors of $\pm 0{\cdot}05$ on $\xi(t)$, which affects the values of $\overline{D}^{GB}_{CaO}\delta$ retrieved by a factor of three at most.

All 10 DIA experiments under intermediate conditions were used to estimate the mean grain boundary diffusivity, $\overline{D}^{GB}_{CaO}\delta$. However, for some experiments performed under dry conditions, the model failed to fit the experimental data satisfactorily. This can be explained by the minor amount of grain growth involved in dry conditions (maximum grain sizes in the reaction rims are typically no larger than tens of nanometers), which is therefore difficult to characterize (see Appendix A). Alternatively, we chose to fit the dry datasets without integrated grain growth; that is, by using the analytical solution given by Abart *et al.* (2009), which allowed us to retrieve mean bulk diffusivity values, $\overline{D}_{CaO}$. Values of grain boundary diffusion, $\overline{D}^{GB}_{CaO}\delta$, were then calculated using equation (12) and an estimated grain size of $l = 120$ nm, based on measurements made on two recovered samples (see Appendix A). The results are listed in Table 2 and, as a test of consistency between the bulk and the microscopic datasets, both are reported on an Arrhenius plot in Fig. 7a, along with $\overline{D}^{GB}_{CaO}\delta$ values from the literature (Fig. 7b). Test analysis of the retrieved diffusion values with varying grain growth parameters, n and ρ, showed that the errors introduced by the estimation of these parameters are negligible compared with other sources of errors (i.e. the initial grain-size distribution and the experimentally determined reaction progress).

For four experiments performed under intermediate conditions and two experiments performed under dry conditions, diffusivities could be retrieved from both the microscopic approach and by simulating kinetic curves (bulk approach). The largest difference observed between the two approaches is 1·33 log units. Although these differences seem significant at first sight, they are within the uncertainties discussed above. In fact, the two datasets show a good consistency between the microscopic (reaction rim and 1D diffusion fronts) and the bulk approaches, as highlighted by the Arrhenius plot in Fig. 7a.

A marked difference is observed between dry and intermediate datasets, where similar values of $\overline{D}^{GB}_{CaO}\delta$ are found at ~823 and 673 K, respectively, similar to the temperature gap observed when comparing bulk reaction kinetics (i.e. half-reaction times; Fig. 4). As for half-reaction times, the diffusivity gap between dry and intermediate conditions seems to shrink towards higher temperatures. The activation energy returned by the Arrhenius fit in the dry case is 573 ± 208 kJ mol^{-1}, which is indeed considerably larger than for the intermediate case (291 ± 29 kJ mol^{-1}). However, in the former case, owing to the narrower temperature range investigated, the uncertainty returned is too large to allow any assertion regarding its absolute value. Conclusively, although our results strongly suggest a larger activation energy in the dry case, they do not entirely exclude the possibility that the activation energy is the same in both cases (i.e. around 300 kJ mol^{-1}).

DISCUSSION

Consistency between bulk and microscopic approaches

To investigate the effect of water on the $MgCO_3 + Ca(OH)_2 \rightarrow Mg(OH)_2 + CaCO_3$ reaction at 1·8 GPa, we designed experiments where the starting material is composed of a grain-size distribution of the first reactant (i.e. magnesite with a log-normal distribution that includes grains $> 10\,\mu m$) reacting with a fine and homogeneous matrix of the second reactant (portlandite $\leq 1\,\mu m$). We show here that this starting material is suitable for the estimation of mean diffusion coefficients from time-resolved *in situ* XRPD provided that (1) significant reaction extents be achieved with sufficient XRD sensitivity, (2) the grain-size distribution of the reactants can be approximated and (3) the texture of the reacted samples can be characterized. Obviously, the conventional approach, which consists in measuring the growth rate of reaction rims, remains more accurate for the determination of diffusion coefficients. However, the *in situ* approach can be appealing in some instances as it allows fast collection of large datasets as required when investigating a range of hydration levels (or a range of pressures) at various temperatures. One obvious limitation of our *in situ* approach with respect to the effect of hydration on reaction kinetics is the absence of a sealed container to ensure constant water concentration over the whole run duration. For example, in the case of the present brucite-bearing system at 1·8 GPa, this limitation implies that the reaction kinetics of samples containing a few thousands of ppm water cannot be reasonably investigated at temperature above *c.* 950 K at the hour timescale (Gasc *et al.*, 2011). The noble metal often used as container material strongly absorbs the X-ray radiation and therefore alters the XRD signal intensity. The use of titanium as capsule material (Chollet *et al.*, 2009) for synchrotron diffraction experiments dealing with water-bearing systems clearly opens the way to the collection of *in situ* XRD data under controlled and constant water content.

Role of the geometry of the intergranular medium

It is important to note that, in the present diffusion dataset, the effect of water content is potentially twofold. Water content will modify the chemistry of the intergranular medium and have an impact on the effective intergranular diffusivity (here $\overline{D}^{GB}_{CaO}$). The presence of water can also modify the geometry of the diffusion paths through grain growth or by controlling the grain boundary width. The impact of grain coarsening on kinetics via the reduction of the intergranular medium available for diffusion can be of several orders of magnitude (Carlson & Gordon, 2004). Therefore, the effect of grain growth has been taken into account by introducing a grain-growth rate law (Appendix A). However, it can be argued that the diffusivity gap between dry and intermediate conditions results from variations of the effective grain boundary width, δ. According to equation (14), identical Ca diffusivity would imply that δ is at least two orders of magnitude greater in intermediate than in dry conditions at 823 K. This seems huge in comparison with what we know about grain boundary width at ambient pressure. Although the effective grain boundary width may be larger than the structural grain boundary width, even in the absence of fluids (Marquardt *et al.*, 2011), in our dry conditions the effective boundary width—which is the one of anhydrous aggregates—should not exceed significantly the structural boundary width, generally described as being equal to a few nanometers (Ricoult & Kohlstedt, 1983; Bons *et al.*, 1990; Farver *et al.*, 1994; Hiraga *et al.*, 1999; Marquardt *et al.*, 2011). On the other hand, studies of water–mineral interface structures show that no more than two monolayers of water are adsorbed at the surface of calcite grains with water being structured over a distance of *c.* 1–5 nm (Fenter & Sturchio, 2004; Cooke *et al.*, 2010). This implies that δ cannot vary by more than one order of magnitude between dry and intermediate conditions. Conclusively, even if intergranular diffusion may be enhanced by small amounts of water through grain boundary widening, this effect alone cannot be responsible for the tremendous differences observed between dry and intermediate cases, which are greater than two orders of magnitude at the lowest temperatures of the present study (Fig. 7a). As suggested by the change in activation energy from intermediate to dry conditions, we are probably documenting here water content dependent diffusion mechanisms, where cation mobility is enhanced by the presence of absorbed water at the grain surfaces (i.e. in the grain boundaries). However, it is possible that even minor amounts of water, such as is the case here, enhance diffusivity not by widening grain boundaries—therefore increasing the structural grain boundary width—but by creating

locally connected porosity (most probably in the form of tubules at triple junctions). This would result in an increased effective grain boundary width, which no longer relates to the actual structural grain boundary width, and the term intergranular diffusion should be preferred over grain boundary diffusion.

We note, however, that so far there has been no systematic measurement of the grain boundary width or structure evolution with increasing pressure. There is, therefore, a clear need for *in situ* experiments that investigate, for example, how confining pressure affects transport properties.

Water content and intergranular Ca-diffusion regimes

The effect of water content on calcium transport (reaction rim growth) derived here is very consistent, at least from a qualitative point of view, with recent work on Mg and Al intergranular transport (Carlson, 2010; Gardés *et al.*, 2012; Milke *et al.*, 2013). In these studies, as in the present one, the addition of small amounts of water, ≤ 1 wt %, was reported to enhance intergranular diffusion by several orders of magnitude, resulting in equal transport properties at temperatures lower by hundreds of degrees. We note that in all cases the activation energies are reported to decrease significantly with increasing water content. The present results are also in good agreement with the results of Gasc *et al.* (2011), where, using a PC set-up that was open with respect to water, a drastic reduction of the electrical conductivity of polycrystalline brucite was observed between samples dried in an oven at 393 K—possibly containing adsorbed water—and samples chemically dried by the addition of CaO. This was also accompanied by an increase of the activation energy of the electrical conductivity from 84 to 106 kJ mol^{-1}. Similarly, the kinetics of the $Ca(OH)_2 + MgCO_3 \rightarrow CaCO_3 + Mg(OH)_2$ exchange reaction, which is also controlled by intergranular transport under the investigated *P–T* conditions, showed a strong positive dependence on water content from dry to saturated conditions (Fig. 4).

In the present study, dry conditions were achieved using chemical drying; that is, by maintaining low water fugacity in the sample with a CaO–$Ca(OH)_2$ solid buffer. The notion of dry conditions may appear somehow contradictory as the dry sample contains hydroxide phases. It should rather be understood in the frame of diffusivity regimes (Farver & Yund, 1995), which were recently redefined by Gardés *et al.* (2012) for enstatite and enstatite + forsterite reaction rims. Those researchers suggested that four regimes can be distinguished as a function of water content, the first regime corresponding to conditions where grain boundaries are essentially anhydrous. The exchange of water between brucite inner grains and grain boundaries observed by Gasc *et al.* (2011) precludes the occurrence of anhydrous grain boundaries in the presence of brucite, as in the present study. Indeed, Milke *et al.* (2013) showed that water content at a tenth of a ppm level is sufficient to switch from anhydrous to hydrous-like reaction textures in orthopyroxene reaction rims at 850–900°C. Hence, the dry conditions obtained here with the addition of CaO cannot correspond to Regime 1 defined by Gardés *et al.* (2012). In addition, the fact that our diffusion data show the least scattering in the dry case (Figs 4 and 7a) suggests that they are relevant to Regime 3, corresponding to hydrous saturated grain boundaries, rather than Regime 2 where diffusivity is expected to be strongly dependent on water content. Regarding our intermediate conditions, although our approach suffers from undetermined water content, the absorbed water on grain surfaces is estimated to represent 1 wt % of the starting material at most, a value that is close to the 0·5 wt % threshold proposed by Gardés *et al.* (2012) for the transition between Regimes 3 and 4 for anhydrous magnesium silicates. In addition, according to Gardés *et al.* (2012), diffusivity variations with water content are also expected to be encountered in Regime 4, where interconnected fluid channels start occurring. This is consistent with the scattering of our diffusivity data for intermediate conditions, as the water content in the sample probably varied from one experiment to the other owing to variable hygrometric conditions and to partial water draining during the experiment. In fact, it might not be fortuitous that the lowest temperature datapoint at 573 K performed under intermediate conditions led to a significantly higher diffusivity value than its counterparts. For this reason, and despite the low uncertainty returned, the (apparent) activation energy for the intermediate conditions should be considered with caution.

Helpa *et al.* (2014) studied experimentally Mg and Ca diffusion in dolomite reaction rims but could not distinguish whether grain boundary or volume diffusion was the dominant process. Farver & Yund (1996) studied Ca grain-boundary diffusion in calcite aggregates. Both studies were performed in anhydrous conditions and their results are compared with ours in Fig. 7b. Extrapolation of the Ca diffusion coefficients obtained in dry conditions to the 750–800°C temperature range indicates that we found higher diffusivity by four and six orders of magnitude than Helpa *et al.* (2014) and Farver & Yund (1996), respectively. This apparent discrepancy can be accounted for by the different water conditions investigated in these two studies, which probably corresponded to Regime 1 (anhydrous), whereas we interpreted our dry experiments as reflecting diffusional Regime 3 defined by Gardés *et al.* (2012). For comparison, we also show in Fig. 7b data for Mg diffusion in enstatite rims of Gardés *et al.* (2012) and Gardés & Heinrich (2011), who respectively investigated Regime 3 and Regime 1. It can be seen that differences of, at least, six orders of magnitude are encountered at 800°C between these two diffusional regimes for $\overline{D}^{GB}_{MgO}\delta$. This comparison with Mg diffusivity in enstatite rims confirms that our dry conditions are consistent with Regime 3.

Interestingly, a major difference between our results and those of Helpa *et al.* (2014) is the unilateral aspect

of the diffusion in our case, where Mg immobility is evidenced, whereas both species (Mg and Ca) were found to diffuse at comparable rates in the experiments of Helpa *et al.* (2014). The difference is even more notable when comparing with the Mg–Ca–Si system, where it has been established that Mg is the most mobile species (Joachim *et al.*, 2011, 2012). Although these differences are admittedly difficult to interpret in terms of diffusion mechanisms, they may well be related to the fact that, in our case, Ca diffuses jointly with H_2O, associated with the breakdown of portlandite upon reaction, which could, in turn, result in faster Ca mobility relative to Mg.

Oxygen diffusivity in the grain boundaries of hot-pressed calcite aggregates was investigated by Farver & Yund (1998) under hydrous conditions (Regime 3). As shown in Fig. 7b, the corresponding $D^{GB}\delta$ values for oxygen under these water conditions lie around our Ca diffusion data under intermediate conditions.

One of the most striking features of Fig. 7b is the location of the Mg intergranular high-temperature diffusivity data (0·1–0·5 and 5 wt % H_2O; i.e. Regime 3 and 4, respectively) derived by Gardés *et al.* (2012). Despite the addition of water, these data lie on the very slow diffusion side of the plot, relatively close to the data for Ca diffusion in anhydrous carbonates (Farver & Yund, 1996; Helpa *et al.*, 2014) and far from hydrous Ca and O diffusion data in carbonates (this study and Farver & Yund, 1996, respectively). We believe that this discrepancy does not rely on the element or oxide that is considered (Mg vs Ca/O) in these studies but rather on the mineralogical–chemical system that was investigated: silicate on the one side and $CaCO_3$ (Farver, 1994; Farver & Yund, 1996), $CaMg(CO_3)_2$ (Helpa *et al.*, 2014) or $CaCO_3$–$Mg(OH)_2$ (this study) on the other side. In the case of volume diffusion, such differences were already pointed out by Farver (1994), who showed that oxygen self-diffusion in non-silicates such as magnetite, apatite and calcite is more than two orders of magnitude larger than in silicates with the same total ionic porosity. In the present case, it is very likely that the hydrated brucite surfaces provide a faster diffusion medium than the silicate ones of Gardés *et al.* (2012), the hydrophobic surface of which probably favors the formation of water pores even at a tenth of a ppm water content level (e.g. Milke *et al.*, 2013). However, in this case, one would expect their experiments performed in Regime 4, with saturated hydrous grain boundaries, to yield diffusion coefficients similar or close to ours, which is far from true, as shown by the data point corresponding to 1 wt % of water from Gardés *et al.* (2012) in Fig. 7b. One major aspect one has to keep in mind when comparing these results is that, unlike for self-diffusion experiments, the diffusion mechanism here, as well as in the study by Gardés *et al.* (2012), is driven by a chemical reaction, as shown by the presence of the ΔG term in our equations (16) and (A5) or in equations (1), (2) and (3) of Gardés *et al.* (2012). The grain boundary diffusivity contrast between our experiments and those of Gardés *et al.* (2012) implies a huge gap between the temperatures required to achieve measurable reaction rims at laboratory timescales (400°C vs 1000°C, respectively). We believe that this highlights the generally well-known difference between reaction kinetics in silicate and carbonate systems, which is often expressed in terms of dissolution rate contrast between rather soluble carbonates and less soluble silicates (Dolejs & Manning, 2010, and references therein). In nature, when intergranular fluids are present and transport is no longer limiting, these solubility differences tend to control the kinetics of metamorphic equilibration (Carlson *et al.*, 2015). We show here that the kinetic contrast between the silicate and carbonate systems seems to hold at very low water contents and even under dry conditions. As a consequence, although the marked effect of low water content (<1 wt %) on intergranular diffusion in mineral aggregates can be understood in the frame of water-sensitive diffusional regimes (Rubie, 1986; Farver & Yund, 1995; Carlson, 2010; Gardés *et al.*, 2012), substantial intergranular diffusivity variations will depend on the chemical and physical properties of the intergranular media, which may differ highly in laboratory experiments and in nature.

Implications for metamorphism

The need for short run duration imposed by the synchrotron beam availability led us to focus on a system characterized by relatively high reaction kinetics, even under dry conditions. Consequently, our experiments significantly departed from nature-relevant kinetics, where slow-diffusing species such as Al control the reaction rate. Our conclusions on the effect of water content are, however, in line with those of Carlson (2010), who, based on natural metamorphic reaction coronae, showed that large gaps exist between aluminum grain boundary diffusivities under 'nearly anhydrous' and 'hydrous but fluid-undersaturated' conditions. Carlson (2010) also suggested an increase of the activation energy of the diffusion from fluid-saturated to anhydrous conditions. Furthermore, it seems that another large diffusivity gap exists as the water content increases and the fluid phase becomes interconnected (Brenan, 1993). Considering the recent study of Gardés *et al.* (2012), which shows the same type of results, it seems that there is a general scheme of diffusivity regimes controlled by water content.

A central question with respect to natural systems is whether water content will affect metamorphic reactions in the temperature range at which they occur. Indeed, the decrease of the activation energy for the diffusion with increasing water content suggests that reaction kinetics are unaffected by water content above a given temperature. In our case, the temperature corresponding to the intersection between the Arrhenius laws determined under dry and intermediate conditions lies at ~1600 K. For the data reported by Carlson (2010) and Gardés *et al.* (2012), this intersection is found at even

higher temperature values. It is therefore likely that the strong effect of water activity (even when less than unity) on reaction kinetics reported here will be relevant to most metamorphic conditions.

In high-grade lower crustal rocks, water activity is mostly expected to be below unity (e.g. Yardley & Valley, 1997) and, therefore, apart from Regime 4, the various diffusivity regimes redefined by Gardés *et al.* (2012) can potentially operate. In dry lower crustal rocks, when hydrous silicates are still present—for example, water activity is close to 10^{-2} (Yardley & Valley, 1997)—this corresponds to what we have called dry conditions here and tentatively interpreted as saturated (or partly saturated) grain boundaries, although in the absence of free fluids. Although our understanding of intergranular transport in water-undersaturated rocks is still very poor, our experiments show that, in lower crustal rocks, grain boundary diffusion rates are rendered much faster by the simple presence of hydrous phases such as brucite. Furthermore, as the addition of minor amounts of water is sufficient to allow transition from Regime 3 to 4, mineral reaction rates are prone to vary by several orders of magnitude with relatively small changes in water activity. It can therefore be emphasized that, as much as temperature, water activity is a first-order parameter that will control reaction rates among minerals. In water-bearing rocks—meaning here rocks that are not anhydrous—the effect of increasing temperature on grain boundary diffusivity will be enhanced by structural water contained in hydrous minerals being progressively transferred into grain boundaries [e.g. Gasc *et al.* (2011) for a laboratory case and Hetenyi *et al.* (2007) for a natural case].

ACKNOWLEDGEMENTS

We are indebted to E. Gardés, W. Carlson and an anonymous reviewer for very constructive reviews that greatly improved the paper. The authors thank G. Hetényi, D. Daval and A. Fernandez-Martinez for valuable discussions.

FUNDING

Université Paris-XI funded J.G.'s PhD grant. Financial support through PROCOPE (grant 09383RJ), HASYLAB and SYSTER (CNRS-INSU) is acknowledged.

REFERENCES

Abart, R., Petrishcheva, E., Fischer, F. D. & Svoboda, J. (2009). Thermodynamic model for diffusion controlled reaction rim growth in a binary system: application to the forsterite–enstatite–quartz system. *American Journal of Science* **309**, 114–131.

Astrom, J. A. (2006). Statistical models of brittle fragmentation. *Advances in Physics* **55**, 247–278.

Austrheim, H. (1987). Eclogitization of lower crustal granulites by fluid migration through shear zones. *Earth and Planetary Science Letters* **81**, 221–232.

Avrami, M. (1939). Kinetics of phase change I—General theory. *Journal of Chemical Physics* **7**, 1103–1112.

Baxter, E. F. (2003). Natural constraints on metamorphic reaction rates. In: Vance, D., Müller, W. & Villa, I. M. (eds) *Geochronology: Linking the Isotopic Record with Petrology and Textures. Geological Society, London, Special Publications* **220**, 183–202.

Berman, R. G. & Aranovich, L. Y. (1996). Optimized standard state and solution properties of minerals. 1. Model calibration for olivine, orthopyroxene, cordierite, garnet, ilmenite in the system FeO–MgO–CaO–Al_2O_3–TiO_2–SiO_2. *Contributions to Mineralogy and Petrology* **126**, 1–24.

Bons, A. J., Drury, M. R., Schryvers, D. & Zwart, H. J. (1990). The nature of grain-boundaries in slates—implications for mass-transport processes during low-temperature metamorphism. *Physics and Chemistry of Minerals* **17**, 402–408.

Brady, J. B. (1983). Intergranular diffusion in metamorphic rocks. *American Journal of Science* **283**, 19.

Brenan, J. M. (1993). Diffusion of chlorine in fluid-bearing quartzite—effects of fluid composition and total porosity. *Contributions to Mineralogy and Petrology* **115**, 215–224.

Brown, W. H., Fyfe, W. S. & Turner, F. J. (1962). Aragonite in California glaucophane schists, and the kinetics of the aragonite–calcite transformation. *Journal of Petrology* **3**, 566–582.

Brunet, F., Bagdassarov, N. & Miletich, R. (2003). $Na_3Al_2(PO_4)_3$, a fast sodium conductor at high pressure: *in-situ* impedance spectroscopy characterisation and phase diagram up to 8 GPa. *Solid State Ionics* **159**, 35–47.

Carlson, W. D. (2010). Dependence of reaction kinetics on H_2O activity as inferred from rates of intergranular diffusion of aluminium. *Journal of Metamorphic Geology* **28**, 735–752.

Carlson, W. D. & Gordon, C. L. (2004). Effects of matrix grain size on the kinetics of intergranular diffusion. *Journal of Metamorphic Geology* **22**, 733–742.

Carlson, W. D., Hixon, J. D., Garber, J. M. & Bodnar, R. J. (2015). Controls on metamorphic equilibration: the importance of intergranular solubilities mediated by fluid composition. *Journal of Metamorphic Geology* **33**, 123–146.

Chollet, M., Daniel, I., Koga, K. T., Petitgirard, S. & Morard, G. (2009). Dehydration kinetics of talc and 10 Å phase: Consequences for subduction zone seismicity. *Earth and Planetary Science Letters* **284**, 57–64.

Christian, J. W. (1975). *Theory of Transformations in Metals and Alloys. I. Equilibrium and General Kinetic Theory*, 2nd edn. Oxford: Pergamon Press, 586 pp.

Cooke, D. J., Gray, R. J., Sand, K. K., Stipp, S. L. S. & Elliott, J. A. (2010). Interaction of ethanol and water with the {1014} surface of calcite. *Langmuir* **26**, 14520–14529.

Decker, D. L. (1971). High-pressure equation of state for NaCl, KCl, and CsCl. *Journal of Applied Physics* **42**, 3239–3244.

Dolejs, D. & Manning, C. E. (2010). Thermodynamic model for mineral solubility in aqueous fluids: theory, calibration and application to model fluid-flow systems. *Geofluids* **10**, 20–40.

Farver, J. R. (1994). Oxygen self-diffusion in calcite—Depen dence on temperature and water fugacity. *Earth and Planetary Science Letters* **121**, 575–587.

Farver, J. R. & Yund, R. A. (1995). Grain-boundary diffusion of oxygen, potassium and calcium in natural and hot-pressed feldspar aggregates. *Contributions to Mineralogy and Petrology* **118**, 340–355.

Farver, J. R. & Yund, R. A. (1996). Volume and grain boundary diffusion of calcium in natural and hot-pressed calcite aggregates. *Contributions to Mineralogy and Petrology* **123**, 77–91.

Farver, J. R. & Yund, R. A. (1998). Oxygen grain boundary diffusion in natural and hot-pressed calcite aggregates. *Earth and Planetary Science Letters* **161**, 189–200.

Farver, J. R., Yund, R. A. & Rubie, D. C. (1994). Magnesium grain-boundary diffusion in forsterite aggregates at 1000°–1300°C and 0·1 MPa to 10 GPa. *Journal of Geophysical Research: Solid Earth* **99**, 19809–19819.

Fenter, P. & Sturchio, N. C. (2004). Mineral–water interfacial structures revealed by synchrotron X-ray scattering. *Progress in Surface Science* **77**, 171–258.

Fisler, D. F. & Mackwell, S. J. (1994). Kinetics of diffusion-controlled growth of fayalite. *Physics and Chemistry of Minerals* **21**, 156–165.

Gardés, E. & Heinrich, W. (2011). Growth of multilayered polycrystalline reaction rims in the MgO–SiO_2 system, part II: modelling. *Contributions to Mineralogy and Petrology* **162**, 37–49.

Gardés, E., Wunder, B., Marquardt, K. & Heinrich, W. (2012). The effect of water on intergranular mass transport: new insights from diffusion-controlled reaction rims in the MgO–SiO_2 system. *Contributions to Mineralogy and Petrology* **164**, 1–16.

Gasc, J., Brunet, F., Bagdassarov, N. & Morales-Florez, V. (2011). Electrical conductivity of polycrystalline $Mg(OH)_2$ at 2 GPa: effect of grain boundary hydration–dehydration. *Physics and Chemistry of Minerals* **38**, 543–556.

German, R. M. (2009). Fragmentation behaviour in particulate materials processing. *Powder Metallurgy* **52**, 196–204.

Helpa, V., Rybacki, E., Abart, R., Morales, L. F. G., Rhede, D., Jerabek, P. & Dresen, G. (2014). Reaction kinetics of dolomite rim growth. *Contributions to Mineralogy and Petrology* **167**, 1001.

Hetenyi, G., Cattin, R., Brunet, F., Bollinger, L., Vergne, J., Nabelek, J. & Diament, M. (2007). Density distribution of the India plate beneath the Tibetan plateau: Geophysical and petrological constraints on the kinetics of lower-crustal eclogitization. *Earth and Planetary Science Letters* **264**, 226–244.

Hiraga, T., Nagase, T. & Akizuki, M. (1999). The structure of grain boundaries in granite-origin ultramylonite studied by high-resolution electron microscopy. *Physics and Chemistry of Minerals* **26**, 617–623.

Joachim, B., Gardés, E., Abart, R. & Heinrich, W. (2011). Experimental growth of akermanite reaction rims between wollastonite and monticellite: evidence for volume diffusion control. *Contributions to Mineralogy and Petrology* **161**, 389–399.

Joachim, B., Gardés, E., Velickov, B., Abart, R. & Heinrich, W. (2012). Experimental growth of diopside plus merwinite reaction rims: The effect of water on microstructure development. *American Mineralogist* **97**, 220–230.

Joesten, R. L. (1991). Kinetics of coarsening and diffusion-controlled mineral growth. In: Kerrick, D. M. (ed.) *Contact Metamorphism. Mineralogical Society of America, Reviews in Mineralogy* **26**, 507–582.

John, T. & Schenk, V. (2003). Partial eclogitisation of gabbroic rocks in a late Precambrian subduction zone (Zambia): prograde metamorphism triggered by fluid infiltration. *Contributions to Mineralogy and Petrology* **146**, 174–191.

Lathe, C., Koch-Muller, M., Wirth, R., van Westrenen, W., Mueller, H. J., Schilling, F. & Lauterjung, J. (2005). The influence of OH in coesite on the kinetics of the coesite–quartz phase transition. *American Mineralogist* **90**, 36–43.

Marquardt, K., Ramasse, Q. M., Kisielowski, C. & Wirth, R. (2011). Diffusion in yttrium aluminium garnet at the nanometer-scale: Insight into the effective grain boundary width. *American Mineralogist* **96**, 1521–1529.

Milke, R., Kolzer, K., Koch-Muller, M. & Wunder, B. (2009). Orthopyroxene rim growth between olivine and quartz at low temperatures (750–950°C) and low water concentration. *Mineralogy and Petrology* **97**, 223–232.

Milke, R., Neusser, G., Kolzer, C. & Wunder, B. (2013). Very little water is necessary to make a dry solid silicate system wet. *Geology* **41**, 247–250.

Molina, J. F., Austrheim, H., Glodny, J. & Rusin, A. (2002). The eclogites of the Marun–Keu complex, Polar Urals (Russia): fluid control on reaction kinetics and metasomatism during high *P* metamorphism. *Lithos* **61**, 55–78.

Mueller, H. J., Schilling, F. R., Lauterjung, J. & Lathe, C. (2003). A standard-free pressure calibration using simultaneous XRD and elastic property measurements in a multi-anvil device. *European Journal of Mineralogy* **15**, 865–873.

Ricoult, D. L. & Kohlstedt, D. L. (1983). Structural width of low-angle grain-boundaries in olivine. *Physics and Chemistry of Minerals* **9**, 133–138.

Rubie, D. C. (1986). The catalysis of mineral reactions by water and restrictions on the presence of aqueous fluid during metamorphism. *Mineralogical Magazine* **50**, 399–415.

Sanchidrian, J. A., Ouchterlony, F., Moser, P., Segarra, P. & Lopez, L. M. (2012). Performance of some distributions to describe rock fragmentation data. *International Journal of Rock Mechanics and Mining Sciences* **53**, 18–31.

Thompson, A. B. (1983). Fluid-absent metamorphism. *Journal of the Geological Society, London* **140**, 533–547.

Wood, B. J. & Walther, J. V. (1983). Rates of hydrothermal reactions. *Science* **222**, 413–415.

Yardley, B. W. D. & Valley, J. W. (1997). The petrologic case for a dry lower crust. *Journal of Geophysical Research: Solid Earth* **102**, 12173–12185.

Zinn, P., Lauterjung, J. & Hinze, E. (1995). Kinetic studies of the crystallization of coesite using synchrotron radiation. *Nuclear Instruments and Methods in Physics Research Section B: Beam Interactions with Materials and Atoms* **97**, 89–91.

APPENDIX A: ESTIMATION OF GRAIN COARSENING PARAMETERS AND IMPLEMENTATION IN THE ANALYTICAL SOLUTION OF ABART *ET AL.* (2009) FOR A SPHERICAL GEOMETRY

Sample PC175, which was obtained under intermediate conditions, exhibits the largest reaction front, which allows the most precise characterization of grain growth among our samples. Measurements of grain size across the reaction front showed that it is proportional to the distance from the Ara + Bru|Mag interface, where the products nucleate (Fig. A1).

This implies that the grain size of the products is proportional to the reaction front width (i.e. $l \propto \Delta x$). Because PC175 is a 1D diffusion experiment, we can consider the relation defined by Gardés & Heinrich (2011) where reaction front growth controlled by grain boundary diffusion obeys

$$\Delta x = A\sqrt{t^{1-1/n}} \tag{A1}$$

where A is a constant and n is the grain growth exponent. At a given temperature, grain growth is known to have an exponential dependence with time of the form

$$l = (\rho t)^{1/n} \tag{A2}$$

where ρ is the growth rate constant. Proportionality between grain size and Δx whatever t implies that $(1 - 1/n)/2 = 1/n$ (i.e. $n = 3$). It should be noted that this is the value of n that was used by Gardés & Heinrich (2011). Then, assuming a value of $n = 3$ for intermediate conditions, ρ could be retrieved for experiments where SEM images allowed measurement of the maximum grain size, l, of the products and using equation (A2). This was done for six intermediate and two dry conditions experiments, respectively. However, under dry conditions, grain growth is limited, with final grain sizes that never exceed 150 nm. In addition, the nucleus size of the reaction products in the reaction rim is unknown. Grain growth in dry conditions was therefore neglected without inducing significant error on the retrieved diffusion values.

The temperature dependence of ρ is of Arrhenius type:

$$\rho = \rho_0 \exp\left(-\frac{Q}{RT}\right) \tag{A3}$$

with $Q = 274$ kJ mol^{-1} and $\rho_0 = 6{\cdot}85 \times 10^{-5}$ m^3 s^{-1} for the intermediate dataset (Fig. A2). Using relation (A3), ρ could be calculated for all DIA experiments run under intermediate conditions and further used to calculate the corresponding $\overline{D}^{GB}_{CaO}\delta$ product as described in the Results section.

To use the grain coarsening model above to retrieve $\overline{D}^{GB}_{CaO}\delta$ in the spherical geometry, differential equation (32) of Abart *et al.* (2009) has been modified to yield the following integral form:

$$\int_1^y y\left\{\frac{y}{[1+u(y^3-1)]^{1/3}} - 1\right\}dy = -\overline{D}^{GB}_{CaO}\delta\frac{\Delta_r G}{RT}\frac{V_m}{V_r}\frac{\pi}{2r_0^2\rho^{1/n}}\int_0^t t^{-1/n}dt. \tag{A4}$$

Noting that $y = 1$ for $t = 0$, we obtain the relation between grain boundary diffusivity, time and rim dimensions for a spherical geometry:

$$\frac{1-y^2}{2} - \frac{1}{2u}\{1-[1+u(y^3-1)]^{2/3}\} = -\overline{D}^{GB}_{CaO}\delta\frac{\Delta_r G}{RT}\frac{V_m}{V_r}\frac{\pi}{2r_0^2\rho^{1/n}}\frac{n}{n-1}t^{(n-1)/n} \tag{A5}$$

where $y = r_B/r_0$.

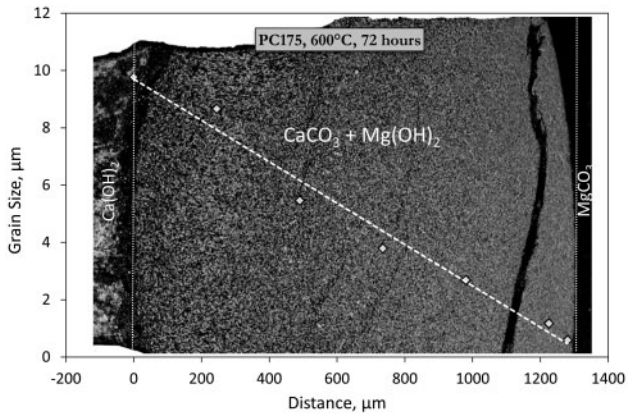

Fig. A1. Grain size of the reaction products across the reaction front in sample PC175. Grain sizes correspond to the average measurement of the five largest identified grains in each location. An SEM backscattered electron image of the reaction front is superimposed to illustrate the grain-size gradient.

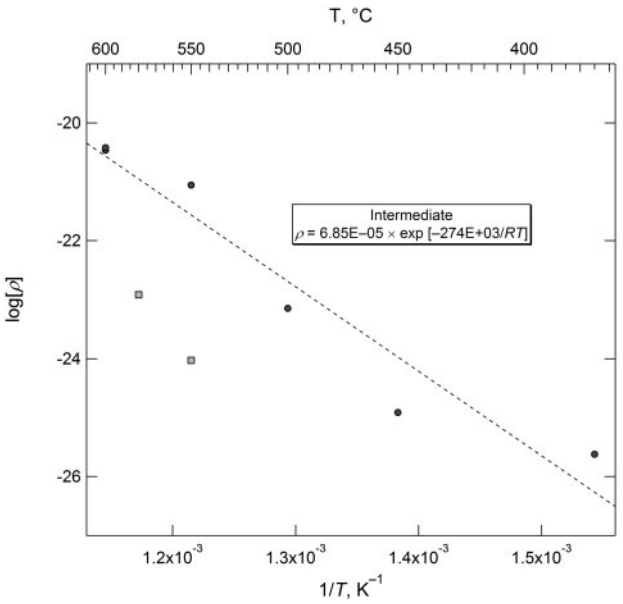

Fig. A2. Arrhenius plot showing the values of ρ obtained from grain-size measurements at various temperatures for intermediate and dry experiments (circles and squares, respectively). The linear regression shown by the dashed line returned the values indicated, according to equation (A3), with Q in J mol^{-1}.

Equation (A5) was used to calculate grain boundary diffusion coefficients based on measurements of r_A and r_B (Fig. 6b). However, using this solution implies calculating first the position of the initial interface r_0. The position of r_0 relative to r_A and r_B can be found assuming that 1 mole of portlandite (i.e. $CaO + H_2O$) entering the rim yields 1 mole of reaction products, $n_m = n_r$, where, again, the brucite + aragonite assemblage is considered as a single phase with a molar volume V_r that is the sum of brucite and aragonite molar volumes. We note that, at any time, the volume of a magnesite grain that has reacted corresponds to $n_m V_m = \frac{4}{3}\pi(r_0^3 - r_B^3)$. Similarly, we can write that the volume of the reaction products corresponds to the volume of the rim, $n_p V_r = \frac{4}{3}\pi(r_A^3 - r_B^3)$. As stated above, the equality between the number of moles on each side leads to the relation

$$\frac{V_M}{V_r} = \frac{r_0^3 - r_B^3}{r_A^3 - r_B^3}. \quad \text{(A6)}$$

The r_0 values were therefore calculated using equation (A6) and then used to retrieve $\overline{D}^{GB}_{CaO}\delta$ values with equation (A5).

APPENDIX B: DEPENDENCE OF DIFFUSIVITY DATA ON THE INPUT GRAIN-SIZE DISTRIBUTION

The distribution of the initial magnesite grain size in our model affects the diffusion coefficient retrieved, simply because finer grains tend to react faster than their coarser counterparts. Although the initial grain-size distribution was partly characterized by SEM images, the consistency between the two parameters that control the grain-size distribution, γ_0 and σ, and the actual magnesite grain dimensions, was tested by a series of simulations. This also allowed us to estimate the errors resulting from approximations made on the aforementioned grain-size distribution.

In the log-normal distribution, γ_0 represents the natural logarithm of the median value, which, based on SEM characterization, was set to 2 μm. The impact of γ_0 on diffusivity was tested for values varying in the range $\exp(\gamma_0) = 1$–5 μm. In the investigated range, the retrieved $\overline{D}^{GB}_{CaO}\delta$ values vary almost linearly with γ_0 (from $1{\cdot}66 \times 10^{-24}$ to $4{\cdot}94 \times 10^{-23}$ m^3 s^{-1} for experiment X11, for example). The parameter σ is also critical as it affects the proportion of large grains present in the sample; it was estimated based on SEM images, which show that large grains, coarser than 20 μm, represent ~30% of the entire magnesite initial volume. This is best modeled with $\sigma = \ln(2{\cdot}5)$. However, we considered here that the uncertainty resulting from the error on σ corresponds to $2{\cdot}2 < \exp(\sigma) < 2{\cdot}9$, which translates into a volume percentage of large grains between ~10 and 50%. It should be noted that this error does not represent an actual variation of grain-size distribution in the starting material but rather the amount of large grains sampled by the X-ray beam, therefore contributing to the overall kinetics. This may vary owing to poor statistics; that is, a handful of large grains only could result in apparently slower kinetics, and, in contrast, if few or no large grains are present, the kinetics will appear to be faster, as they will be mainly controlled by the reaction of small grains. The results of these tests show that, for experiment X11 for example, when $\exp(\sigma)$ varies from 2·2 to 2·9, the obtained values of $\overline{D}^{GB}_{CaO}\delta$ vary from $2{\cdot}80 \times 10^{-24}$ to $2{\cdot}25 \times 10^{-23}$ m^3 s^{-1}. It should be noted here that we expect the grain-size distribution in the starting material to be similar in all experiments and, therefore, errors discussed above should not affect the variations of $\overline{D}^{GB}_{CaO}\delta$ observed with water content and temperature.